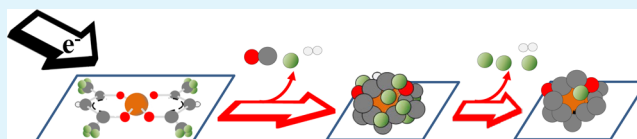# Electron Induced Surface Reactions of Organometallic Metal(hfac)$_2$ Precursors and Deposit Purification

Samantha G. Rosenberg, Michael Barclay, and D. Howard Fairbrother*

Department of Chemistry, Johns Hopkins University, Baltimore, Maryland 21218, United States

Ⓢ *Supporting Information*

ABSTRACT: The elementary processes associated with electron beam-induced deposition (EBID) and post-deposition treatment of structures created from three metal^{II}(hfac)$_2$ organometallic precursors (metal = Pt, Pd, Cu; hfac = CF$_3$C(O)CHC(O)CF$_3$) have been studied using surface analytical techniques. Electron induced reactions of adsorbed metal^{II}(hfac)$_2$ molecules proceeds in two stages. For comparatively low electron doses (doses <1 × 10^{17} e$^-$/cm^2) decomposition of the parent molecules leads to loss of carbon and oxygen, principally through the formation of carbon monoxide. Fluorine and hydrogen atoms are also lost by electron stimulated C−F and C−H bond cleavage, respectively. Collectively, these processes are responsible for the loss of a significant fraction (≥50%) of the oxygen and fluorine atoms, although most (>80%) of the carbon atoms remain. As a result of these various transformations the reduced metal atoms become encased in an organic matrix that is stabilized toward further electron stimulated carbon or oxygen loss, although fluorine and hydrogen can still desorb in the second stage of the reaction under the influence of sustained electron irradiation as a result of C−F and C−H bond cleavage, respectively. This reaction sequence explains why EBID structures created from metal^{II}(hfac)$_2$ precursors in electron microscopes contain reduced metal atoms embedded within an oxygen-containing carbonaceous matrix. Except for the formation of copper fluoride from Cu^{II}(hfac)$_2$, because of secondary reactions between partially reduced copper atoms and fluoride ions, the chemical composition of EBID films and behavior of metal^{II}(hfac)$_2$ precursors was independent of the transition metal's chemical identity. Annealing studies of EBID structures created from Pt^{II}(hfac)$_2$ suggest that the metallic character of deposited Pt atoms could be increased by using post deposition annealing or elevated substrate temperatures (>25 °C) during deposition. By exposing EBID structures created from Cu^{II}(hfac)$_2$ to atomic oxygen followed by atomic hydrogen, organic contaminants could be abated without annealing.

KEYWORDS: *EBID, FEBIP, organometallic, hfac, purification, radical*

1. INTRODUCTION

Electron beam-induced deposition (EBID) of volatile organometallic precursors is a vacuum-based, site-selective, single-step lithographic technique capable of making and prototyping three-dimensional, metal-containing nanostructures in electron microscopes without masks or resists.[1−4] A number of different metals can be deposited using organometallic precursors developed for thermal deposition processes such as chemical vapor deposition (CVD), enabling EBID deposits to be tailored for particular applications. For example, Pt or Cu containing precursors (e.g., MeCpPtMe$_3$, (hfac)Cu^I(vinyltrimethylsilane)) are preferred for the growth of metallic nanowires or in electronic applications,[5−8] whereas Co or Fe containing precursors (e.g., Co(CO)$_3$NO, Co$_2$(CO)$_8$ and Fe(CO)$_5$) are used to create magnetic nanostructures.[9−13] EBID has also been used to create AFM tips,[10,14] catalyst nanoparticles for growing CNT's,[15,16] magnetic nano-Hall sensors,[11] electrical contacts,[17] and in mask repair.[18,19]

Every organometallic precursor contains organic ligands attached to the central metal atom. These ligands can be subdivided into monodentate ligands, such as CO and CH$_3$, that are attached to the central metal atom through a single metal−ligand bond, and multidentate ligands, such as

hexafluoroacetylacetonate (hfac; CF$_3$C(O)CHC(O)CF$_3$), which are bonded to the central metal atom through multiple ligand−metal bonds. Among the bidentate ligands, hfac is one of the most widely used because it can form metal−ligand bonds with transition metals that do not form stable carbonyls, such as platinum, palladium, and copper.[20] Cu^{II}(hfac)$_2$ has been used in EBID to make deposits for high-performance integrated circuits in an attempt to combine the selective deposition afforded by EBID with copper's low-cost and lower electrical resistivity compared to Si or Al.[21−23]

Despite the relative ease and flexibility of structures that can be created by EBID, a number of scientific and technological challenges are preventing EBID from reaching its full potential as a robust tool for nanofabrication. One of the major drawbacks is the often unacceptably high level of organic contamination, particularly carbon, contained within the deposits. This contamination negatively impacts the deposit's properties (e.g., by increasing resistivity or decreasing catalytic activity) and therefore limits the range of potential applications

for metal-containing EBID nanostructures. Ligand decomposition is the principal source of organic contamination in EBID. Thus, although $Cu^{II}(hfac)_2$, $Pd^{II}(hfac)_2$ and $Pt^{II}(hfac)_2$ can all produce pure metal films in thermal deposition processes such as CVD,[24] nanostructures created by EBID from hfac-containing precursors exhibit high carbon contents and correspondingly low metal purity. For example, Luisier et al., have reported nanostructures created from $Cu^{II}(hfac)_2$ with very low metal contents (14% Cu), and a correspondingly high carbon content (75% C).[22] Similarly, Miyazoe et al. reported that deposits created by EBID from $Cu^{II}(hfac)_2$ exhibit only 11−12% Cu content.[23] These limitations with existing CVD precursors have provided the impetus to better understand the fundamental bond breaking processes involved in EBID. The goal is to provide information that can be used to design new, EBID specific precursors capable of creating nanostructures with improved metal content.

Given the typically low metal content (often <20%) in EBID structures, several different approaches have been evaluated for their ability to abate the organic contamination. These strategies have included varying the deposition conditions (i.e., changing the current, energy, or dwell time of the electron beam), and heating the substrate to elevated temperatures either during or after deposition.[1,6,12,25,26] An alternative strategy has been to expose deposits to reactive species capable of volatilizing organic contaminants.[27] For example, Miyazoe et al. reported that when EBID deposits created from $Cu^{II}(hfac)_2$ were treated with a hydrogen−argon plasma, the Cu content could be increased from 11 to 12% to 27%.[23] In related studies, Wnuk et al. have observed that when EBID films created from dimethyl(acetylacetonate)gold(III) ($Me_2Au(acac)$) were exposed to atomic oxygen (AO) and then atomic hydrogen (AH), almost all of the carbon was removed, creating pure gold deposits.[28]

As a step toward developing a more detailed fundamental understanding of the electron stimulated reactions of $metal^{II}(hfac)_2$ compounds, Engmann et al., have recently explored the interactions of low energy (0−12 eV) electrons with gas phase $Cu^{II}(hfac)_2$, $Pd^{II}(hfac)_2$.[29] Motivation for these studies derives from the widespread belief that in the EBID process, precursor dissociation is initiated by the low energy secondary electrons produced by the interactions of the high-energy primary beam with the substrate.[30,31] These gas phase studies showed that $Cu^{II}(hfac)_2$ predominately undergoes nondissociative electron attachment (NDEA) to form $Cu^{II}(hfac)_2^-$, whereas for $Pd^{II}(hfac)_2$, the precursor's preferred reaction pathway is the loss of $(hfac)^-$.[29] The authors postulated that this difference occurs because the open shell $Cu^{II}(hfac)_2$ (17 electrons) is more likely to be stabilized by the addition of an extra electron to form $Cu^{II}(hfac)_2^-$ compared to the filled shell $Pd^{II}(hfac)_2$ (18 electrons).[29]

Over the past several years, we have developed an ultrahigh vacuum (UHV), surface science approach to acquire more detailed molecular level information on the EBID process.[28,32−40] These surface science studies on adsorbed organometallic precursors represent an increasing level of complexity compared to gas phase studies and provide a bridge between information that can be obtained from typical EBID studies, primarily conducted in electron microscopes, and data on the reactions of electrons with isolated precursor molecules in the gas phase. Thus, UHV surface science studies can track the electron-stimulated decomposition of organometallic precursors in situ, identify the volatile species created during

deposition, and study the effects of post-deposition purification strategies. In the present study, we have used this approach to interrogate the electron stimulated surface reactions of the different $metal^{II}(hfac)_2$ precursors, specifically platinum(II) hexafluoroacetylacetonate ($Pt^{II}(hfac)_2$), copper(II) hexafluoroacetylacetonate ($Cu^{II}(hfac)_2$), and palladium(II) hexafluoroacetylacetonate ($Pd^{II}(hfac)_2$). Results from these studies have been used to determine the bond breaking processes involved in deposition and the extent to which these processes are similar or differ among the three different precursors. As part of our investigation, we have also examined the effects of two different post-deposition abatement strategies, specifically substrate heating and exposure to atomic radicals, on the bonding and composition in EBID films created from $Pt^{II}(hfac)_2$ and $Cu^{II}(hfac)_2$.

2. EXPERIMENTAL SECTION

Precursors. Copper(II) hexafluoroacetylacetonate ($Cu^{II}(hfac)_2$; CAS 14781−45−4, Strem Chemicals, Inc.), Palladium(II) hexafluoroacetylacetonate ($Pd^{II}(hfac)_2$; CAS 64916−48−9, Strem Chemicals, Inc.), and Platinum(II) hexafluoroacetylacetonate ($Pt^{II}(hfac)_2$; CAS 65353−51−7, Strem Chemicals, Inc.) exist as blue, yellow, and orange crystals, respectively, at standard temperature and pressure (STP). All three precursors were added into glass fingers that were attached to a gas manifold. Each precursor was admitted into the two UHV chambers after the gas manifold had been evacuated into the mTorr pressure regime by a mechanical pump and the precursor subsequently heated to ≈50−70 °C.

Two types of experiments were conducted in two different UHV chambers, whose analytical capabilities have been described in previous publications.[32,34,38,40,41] The bulk of the experiments reported in this study were carried out in situ with X-ray photoelectron spectroscopy (XPS) and mass spectrometry (MS) to study the effect of electron irradiation on adsorbed $Pt^{II}(hfac)_2$, $Cu^{II}(hfac)_2$ and $Pd^{II}(hfac)_2$ molecules as well as the effect of annealing on EBID structures created from $Pt^{II}(hfac)_2$. The second UHV chamber, an AES system (PHI 610) modified by the addition of a thermal cracker was used to study the composition of films grown by EBID from $Cu^{II}(hfac)_2$, $Pd^{II}(hfac)_2$ and $Pt^{II}(hfac)_2$ under steady-state deposition conditions as well as the effect of atomic radicals on EBID structures created from $Cu^{II}(hfac)_2$.

Brief descriptions of the various experimental elements are provided in the following sections.

XPS/MS Experiments. *Creating Films.* Films of nanometer thicknesses were created on 1 cm² substrates by introducing the precursor gases onto cooled 1 cm² substrates with no electron irradiation present. The average thicknesses of the films created from the precursor in this way were, $Cu^{II}(hfac)_2$ (2.0−2.5 nm), $Pd^{II}(hfac)_2$ (>5.0 nm), and $Pt^{II}(hfac)_2$ (3.8−4.2 nm). Experiments with $Pt^{II}(hfac)_2$ were conducted on a Au substrate cooled to −168 °C, while studies on $Cu^{II}(hfac)_2$ and $Pd^{II}(hfac)_2$ were conducted on an amorphous carbon (a:C) substrate (created by Ar⁺ sputtering HOPG) cooled to −110 °C. For $Cu^{II}(hfac)_2$ and $Pd^{II}(hfac)_2$ experiments were performed on a:C because there was evidence that these two molecules underwent partial decomposition on Au. For example, in the case of $Cu^{II}(hfac)_2$, metallic Cu peaks were observed in the XPS even at low deposition temperatures, consistent with previous studies by Lin et al.[42]

$Pt^{II}(hfac)_2$ was preferred for detailed XPS analysis because of spectroscopic issues with $Pd^{II}(hfac)_2$ and $Cu^{II}(hfac)_2$. In the case of $Pd^{II}(hfac)_2$, this was due to overlap between the $Pd(3p_{3/2})$ and $O(1s)$ peaks,[43] whereas for $Cu^{II}(hfac)_2$, unambiguous deconvolution of the $Cu(2p)$ region is extremely difficult. However, a sufficient number of complementary experiments were performed with $Pd^{II}(hfac)_2$ and $Cu^{II}(hfac)_2$ to allow us to compare the reactivity among the three $M^{II}(hfac)_2$ precursors.

For XPS experiments on $Pt^{II}(hfac)_2$, film thicknesses were determined by measuring the attenuation of the $Au(4f)$ signal.[44] $Cu^{II}(hfac)_2$ film thicknesses on the a:C substrates were determined
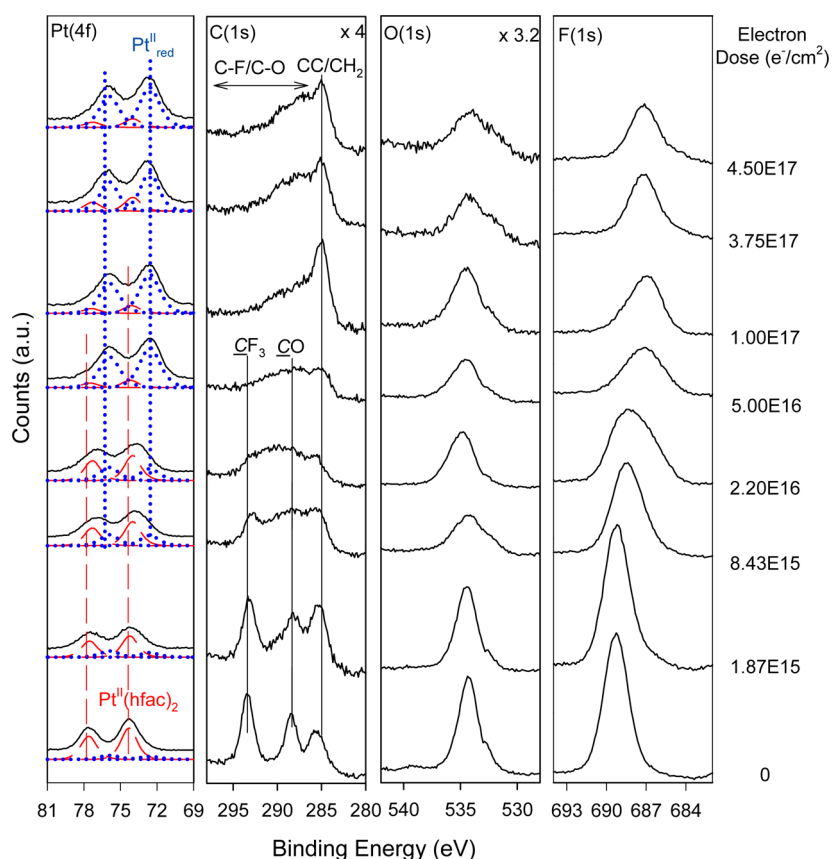
Figure 1. Evolution of the Pt(4f), C(1s), O(1s), and F(1s) XP regions for 3.6−4.2 nm thick films of $Pt^{II}(hfac)_2$ as a function of increasing electron dose. Films were adsorbed onto a gold substrate at −168 °C and the incident electron energy was 500 eV. The corresponding electron dose is shown on the right-hand side of each set of spectra. Fits are included in the Pt(4f) region for the parent (red, dashed lines) and product (blue, dotted lines) species. All XP spectra were recorded with a step size of 0.125 eV and at pass energies of 22 eV.

from the attenuation of the C−C peak associated with the a:C substrate. The more limited number of experiments performed with $Pd^{II}(hfac)_2$ were conducted on sufficiently thick (>5.0 nm) films that there was no longer a contribution to the C(1s) spectra from the a:C substrate.[38,40,41]

Electron Source. Once the film's thickness and composition were determined by XPS, it was exposed to a known electron dose oriented at normal incidence to the sample surface. For all MS and XPS experiments a commercial flood gun (Specs FG 15/40) was used as a broad beam electron source.[34,38] An incident electron energy of 500 eV was used throughout, calculated from the sum of the electron energy generated by the flood gun (480 eV) and a positive bias (+20 V) applied to the substrate to prevent the majority of secondary electrons produced during irradiation from escaping. The target current was held at 5 μA, unless noted. Electron irradiation is reported in terms of dose (e⁻/cm²).

AES Experiments. *Creating EBID Films.* The $metal^{II}(hfac)_2$ precursor was directed onto the substrate through a directional doser, while the Auger electron beam was rastered across the surface for a prescribed period of time. The pressure of precursor molecules at the surface was held constant during deposition by monitoring the chamber pressure, as was the target current. Film thicknesses were not measured, but each deposit was sufficiently thick to obscure the AES signal from the underlying Au substrate. To ensure that deposition was defined by the electron beam (i.e., it was created by EBID), the two-dimensional nature of the films was checked using a secondary electron detector (SED).

Electron Source. For all AES experiments a 3 keV electron beam was created from a LaB6 filament cathode and rastered over ≈1.5 μm spot size and a power density of ∼2 × 10² μW/μm².

Radical Treatment. The effect of atomic radicals on EBID structures created from $Cu^{II}(hfac)_2$ was studied in situ. Atomic

radicals were generated by flowing oxygen or hydrogen gas through a thermal gas cracker (Oxford Applied Research) to produce a directed flux of atomic radicals (80−90% dissociation efficiency based on manufacturer's estimate).[28]

The chemical composition of EBID films was determined by AES. Using the AugerMap software, spatial concentration maps of surface copper, carbon, fluorine, and oxygen atoms were also obtained by measuring the difference in AES signals between their respective Auger transitions (CuLMM ≈ 920 eV, CKLL ≈ 262 eV, FKLL ≈ 647 eV, OKLL ≈ 503 eV) and a proximate electron energy that corresponded to the background signal.

3. RESULTS

Figure 1 shows the evolution in the Pt(4f), C(1s), O(1s), and F(1s) regions measured by XPS for 3.6−4.2 nm thick $Pt^{II}(hfac)_2$ films as a function of increasing electron dose. Control studies (shown in Figure S1 in the Supporting Information) used to determine the sensitivity of the adlayer to the secondary electrons generated during XPS analysis revealed that 161 min of total X-ray exposure produce relatively small changes to the Pt(4f), C(1s), O(1s) regions, most notably a loss in the CF_3 group intensity and a slight broadening of the C(1s) region. Despite this relative insensitivity, each film was only exposed to X-ray irradiation after deposition and then again after a single electron dose, collectively corresponding to a total of ∼70 min of X-ray exposure. Thus, changes in the XPS shown in Figure 1 are dominated by the effect of the 500 eV electrons generated by the electron gun.

Analysis of the evolution in Pt(4f), C(1s), O(1s), and F(1s) regions exposed to electron radiation and corresponding changes to the atom concentration (see Figure 2) reveals two
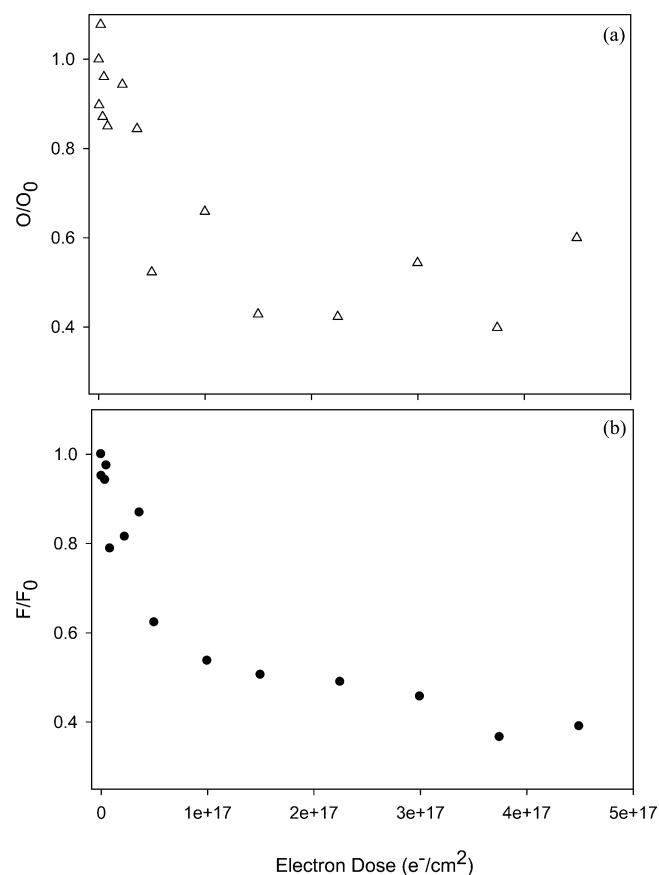

Figure 2. Change in the fractional coverage of adsorbed (a) oxygen and (b) fluorine atoms for 3.6−4.2 nm $Pt^{II}(hfac)_2$ films exposed to electron irradiation, plotted as a function of electron dose. Each relative concentration (F/F_0, O/O_0) was determined by XPS with the initial F_0, and O_0 values measured on the $Pt^{II}(hfac)_2$ film prior to electron irradiation. Films were adsorbed onto Au substrates at −168 °C and exposed to 500 eV electrons.

regimes of transformation; those that occur for electron doses $\leq 1 \times 10^{17}$ e$^-$/cm^2 and then for $\geq 1 \times 10^{17}$ e$^-$/cm^2. Prior to irradiation, the Pt(4f) region contains a Pt($4f_{7/2}/4f_{5/2}$) doublet (Pt($4f_{7/2}$) peak position = 74.3 eV) associated with adsorbed $Pt^{II}(hfac)_2$ molecules (shown as dashed lines in Figure 1). For electron doses $\leq 1 \times 10^{17}$ e$^-$/cm^2, the Pt(4f) region broadens to a lower binding energy and the resulting envelope can be well fit using contributions from parent $Pt^{II}(hfac)_2$ molecules and a new Pt($4f_{7/2}/4f_{5/2}$) doublet with a Pt($4f_{7/2}$) peak at 72.6 eV. This new component is indicated by dotted lines in Figure 1 with the Pt($4f_{7/2}$) peak identified at Pt$_{red}$. For electron doses $\geq 1 \times 10^{17}$ e$^-$/cm^2, the Pt(4f) spectral envelope is dominated by the Pt$_{red}$ species with little or no contribution from the Pt($4f_{7/2}/4f_{5/2}$) doublet associated with the parent $Pt^{II}(hfac)_2$ molecules. The decrease (>1.5 eV) that occurs to the Pt(4f) binding energy as a result of electron irradiation is most apparent by comparing the bottom two spectra in Figure 6a, which shows the measurable change in Pt(4f) binding energy that occurs as the Pt($4f_{7/2}/4f_{5/2}$) molecules are decomposed by electron irradiation.

The C(1s) region prior to electron exposure consists of three well-defined peaks, centered at 285.5, 288.5, and 293.6 eV, due to the CH, CO and CF_3 carbon atoms in the hfac ligand, respectively.[21] For electron doses $<1 \times 10^{17}$ e$^-$/cm^2, the well-defined peak structure is degraded and the CF_3 peak disappears. For electron doses $>1 \times 10^{17}$ e$^-$/cm^2, the dominant transformation is an increase in concentration of the graphitic like CC/CH_2 species at the expense of the CF and CO species (see also Figure S2 in the Supporting Information for the effect of electron irradiation on $Pd^{II}(hfac)_2$ films), although the integrated area of the C(1s) region decreases by only 10−20% over the course of electron exposure. Consequently, the dominant transformation that occurs to carbon atoms involves changes to the local bonding environments as opposed to desorption. Prior to irradiation, the O(1s) region consists of a dominant peak at 534.5 eV due to the CO species in the hfac ligand.[21] For electron doses $\leq 1 \times 10^{17}$ e$^-$/cm^2, changes in the O(1s) region are dominated by a loss of ~50% spectral intensity while for electron doses $\geq 1 \times 10^{17}$ e$^-$/cm^2 the intensity in the O(1s) region remains relatively unchanged (see Figure 2(a)). Initially, the F(1s) region also consists of a single peak (at 689.3 eV) due to the CF_3 species in the hfac ligand.[21] For electron doses $\leq 1 \times 10^{17}$ e$^-$/cm^2, there is a pronounced loss of intensity (~50%) and a small decrease in binding energy. At higher electron doses $\geq 1 \times 10^{17}$ e$^-$/cm^2, the F(1s) region continues to lose intensity, albeit at a slower rate (Figure 2b).

Figure 3a shows a comparison of the neutral gas phase species produced when, (i) gas phase $Pt^{II}(hfac)_2$ molecules were exposed to 70 eV electrons in the quadrupole MS and, (ii) adsorbed $Pt^{II}(hfac)_2$ molecules were irradiated by 500 eV electrons. Analysis of Figure 3a,i reveals that the MS of gas phase $Pt^{II}(hfac)_2$ yields significant peaks for CF_3, CO, F, O, and C, with smaller contributions from CF_2, CFO, CO_2, and H_2. Although the authors were not able to find any mass spectra data for the $Pt^{II}(hfac)_2$ precursor, the cracking pattern in Figure 3a is analogous to published mass spectra data on the $Cu^{II}(hfac)_2$ precursor.[45] Figure 3a,ii shows that when adsorbed $Pt^{II}(hfac)_2$ molecules are electron irradiated, the volatile neutrals produce significant peaks for CO, O, C, and H_2, with smaller contributions from CO_2. Indeed, the ratio of CO:O:C is consistent with the fragmentation pattern for CO. Therefore, a notable contrast to the gas phase $Pt^{II}(hfac)_2$ spectra in Figure 3a,i is that no fluorine-containing species (e.g., CF_3, CF_2, CFO, etc.) are observed in Figure 3a,ii. Figure 3b shows the kinetics of electron stimulated CO evolution from adsorbed $Pt^{II}(hfac)_2$ molecules (solid circles - left-hand axis). Figure 3b also shows how the fractional concentration of oxygen atoms volatilized from $Pt^{II}(hfac)_2$ during electron irradiation changes as a function of electron dose. Because Figure 2a shows that ~50% of the nascent oxygen atoms are lost from adsorbed $Pt^{II}(hfac)_2$ films as a result of electron irradiation, this is plotted as ($O/O_0 - 0.5$) (left-hand axis— open circles). Analysis of Figure 3b shows that the gas phase CO evolution and loss of oxygen from the surface follow the same kinetic dependence on electron dose.

Figure 4 details the effect of electron exposure on the F(1s) XP region of a $Cu^{II}(hfac)_2$ film. Prior to electron irradiation, the F(1s) region, is characterized by one peak at 688.6 eV, consistent with Figure 1. However, in contrast to the evolution of the F(1s) region of $Pt^{II}(hfac)_2$ or $Pd^{II}(hfac)_2$ films the decrease in C−F peak intensity that occurs with increasing
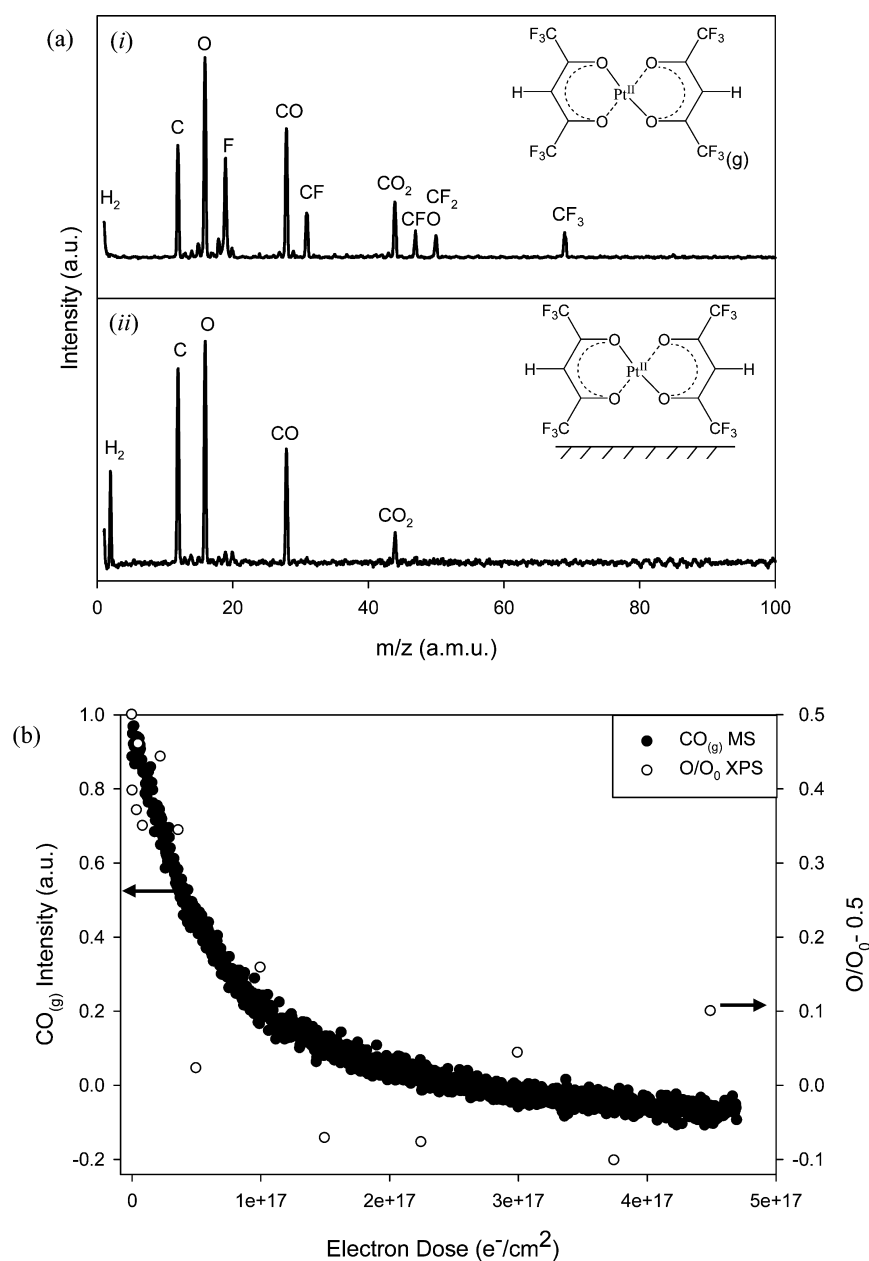
8593

dx.doi.org/10.1021/am501457h | ACS Appl. Mater. Interfaces 2014, 6, 8590−8601

Figure 3. (a) Mass spectrum (0−100 amu) of (i) gas phase $Pt^{II}(hfac)_2$ measured at $P_{Pt(hfac)_2} \approx 6.0 \times 10^{-7}$ Torr, (ii) the volatile neutral species produced when a ∼ 4.0 nm film of $Pt^{II}(hfac)_2$, adsorbed onto a gold substrate at −168 °C was irradiated by an electron dose of 2.40×10^{17} e$^-$/cm^2 (incident energy of 500 eV); the spectrum represents an average of MS taken every 20 s during the electron exposure. (b) Effect of electron dose on (filled circles) partial pressure of gas phase CO evolved from a $Pt^{II}(hfac)_2$ film, (open circles) change in the labile oxygen atom concentration in the film ($O/O_0 − 0.5$). Both data sets were acquired for 3.6−4.2 nm $Pt^{II}(hfac)_2$ films (incident electron energy 500 eV).

electron dose is accompanied by the appearance of a distinct new peak at 686.0 eV, indicative of a fluoride ion (F$^-$).[46]

Figure 5a−c shows the in situ AE spectra of 500 μm × 360 μm structures deposited by EBID in the AES system using a constant partial pressure of (a) $Cu^{II}(hfac)_2$, (b) $Pd^{II}(hfac)_2$, and (c) $Pt^{II}(hfac)_2$ ($P_{M(hfac)_2} \approx 1.5-3.0 \times 10^{-7}$ Torr). Figure 5a−c show that the Auger spectra contain transitions associated with their respective metals: Cu (920 eV, 849 eV, 776 eV), Pd (330 eV) and Pt (64 eV). A discernible oxygen peak (503 eV) is also present but all of the Auger spectra are dominated by a large carbon (272 eV) peak. The most significant difference between the three structures is that the Cu^{II}(hfac)$_2$ displays a prominent

F peak (647 eV), which is noticeably absent for the $Pt^{II}(hfac)_2$ and barely visible for $Pd^{II}(hfac)_2$.

Figure 6 shows the effect of annealing an EBID film initially created by exposing $Pt^{II}(hfac)_2$ molecules to an electron dose of 4.50×10^{17} e$^-$/cm^2. On the basis of the data in Figure 1 this electron dose is sufficient to decompose all of the parent $Pt^{II}(hfac)_2$ molecules, but insufficient to remove all of the nascent fluorine atoms. Figure 6a describes the effect of electron irradiation and subsequent annealing on the $Pt(4f_{7/2})$ peak position. The initial electron dose used to generate the EBID structure causes the $Pt(4f_{7/2})$ peak position to decrease by 1.7 eV, from 74.3 to 72.6 eV, as shown in Figure 1. When the film is subsequently annealed to room temperature the
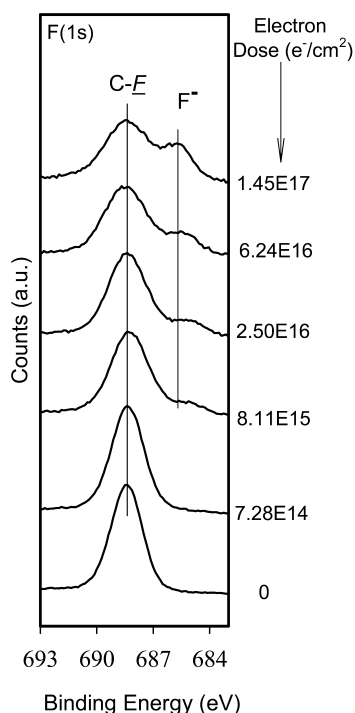
Figure 4. Evolution of the F(1s) XP region as a function of electron dose for 2.0−2.5 nm thick films of $Cu^{II}(hfac)_2$ adsorbed onto an (a:C) substrate at −100 °C (dose shown on right-hand side).
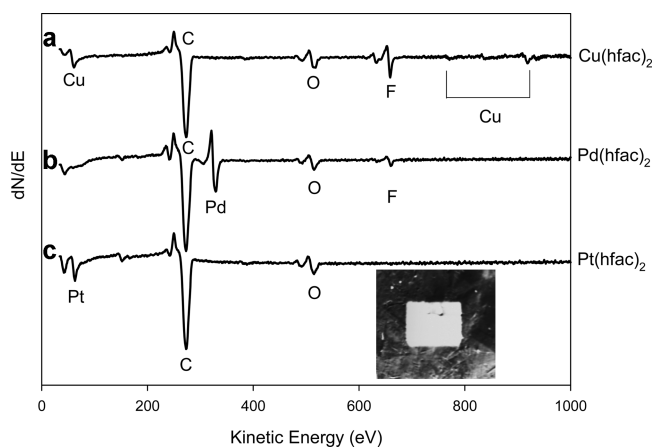
Figure 5. Auger electron spectra of EBID structures created from (a) $Cu^{II}(hfac)_2$, (b) $Pd^{II}(hfac)_2$, and (c) $Pt^{II}(hfac)_2$ on a Au substrate. Deposition conditions were $P_{precursor} \approx$ 1.5- 3.0 × 10^{-7} Torr, incident beam energy =3 keV, substrate current ≈1- 2 μA for a total electron dose of: ~ 4.7 × 10^{18} e⁻/cm^2. Inset shows an SEM image of the $Pt^{II}(hfac)_2$ structure.

Pt(4f$_{7/2}$) peak position remains unchanged although at higher annealing temperatures the Pt(4f$_{7/2}$) peak systematically decreases, reaching a binding energy of 71.6 eV at 367 °C. This value is close to that of bulk platinum (71.2 eV).[43] Figure 6b shows the variation in intensity within the Pt(4f), C(1s), F(1s), and O(1s) regions of the EBID film as a function of annealing temperature. The platinum, carbon and fluorine signals remain unchanged. The oxygen signal, however, decreases steadily above 120 °C and is barely perceptible (<5%) at annealing temperatures above 300 °C.

Figure 7a−c show the in situ AE spectra of: (a) a rectangular EBID structure deposited in the AES system from $Cu^{II}(hfac)_2$,

(b) the same structure after 40 h exposure to atomic oxygen and (c) subsequently exposed to 2 h of atomic hydrogen. Figure 8 shows the corresponding AES maps. Figures 7a and 8a show that the native EBID structure is characterized by the presence of: Cu (920, 849, 776 eV), C (272 eV), O (503 eV), and F (647 eV) Auger peaks. Following 40 h of atomic oxygen exposure, the carbon and fluorine has all but disappeared with a concomitant increase in intensity of the oxygen and copper AES peaks (Figures 7b and 8b). After this structure was subsequently exposed to atomic hydrogen for 2 h, the oxygen signal decreased drastically, with a corresponding increase in the Cu AES signal (Figures 7c and 8c). The combination of atomic oxygen followed by atomic hydrogen treatment therefore produces a structure dominated by Cu AES peaks.

4. DISCUSSION

Electron Stimulated Reactions. Figures 1−3 show that electron irradiation of adsorbed $Pt^{II}(hfac)_2$ molecules changes the chemical composition and/or bonding environment for the platinum, carbon, fluorine, and oxygen atoms. The majority of changes in bonding and atom concentration occur for electron doses <1 × 10^{17} e⁻/cm^2. These include the loss of parent Pt(+2) species from $Pt^{II}(hfac)_2$ into a more reduced form of platinum (Pt$_{red}$) which exhibits a binding energy (72.6 eV) intermediate between Pt atoms in $Pt^{II}(hfac)_2$ and metallic Pt (≈ 71.2 eV).[43] Similar changes in Pt(4f$_{7/2}$) binding energies have also been observed for other Pt precursors, MeCpPtMe$_3$ and Pt(PF$_3$)$_4$, exposed to electron irradiation.[32,38] The loss of significant amounts of both oxygen and fluorine from the surface also occurs during this initial period of irradiation. Indeed, all of the oxygen loss (≈ 50% of the initial content) occurs for electron doses <1 × 10^{17} e⁻/cm^2. Moreover, Figure 3b shows that there is a correlation between the rate at which volatile oxygen atoms are lost from the surface and the rate of gas phase CO production. From this, we conclude that oxygen is lost predominantly in the form of CO$_{(g)}$, possibly accompanied by a small amount of CO$_2$(g) (see Figure 3). Based on the chemical structure of the hfac ligands (CF$_3$C-(O)CHC(O)CF$_3$), it appears that approximately half of the C=O groups in the precursor molecules are ejected into the gas phase. The concomitant loss of fluorine atoms from the film is evidenced by the decrease in the F(1s) peak intensity and the CF$_3$ peak in the C(1s) envelope, shown in Figures 1 and 2b. However, the loss of fluorine from the surface is not accompanied by the appearance of any fluorine or carbon−fluorine containing fragments (e.g., F, CF, CFO) in the neutral gas phase species ejected during the electron irradiation of $Pt^{II}(hfac)_2$ films (Figure 3a(ii)). This suggests that fluorine atoms desorb predominantly in the form of F⁻(g) because of electron-stimulated C−F bond cleavage (C−F(ads) + e⁻ ⇒ C·(ads) + F⁻(g)), a process that has been shown to be important for fluoropolymers or fluorine-containing thin films (e.g., SAMs) exposed to electrons or ionizing radiation.[47−52] Because electron-stimulated C−F bond cleavage does not result in any carbon desorption, CO and possibly CO$_2$ are the only volatile carbon-containing species produced. These observations explain why electron irradiation leads to significant losses of oxygen and fluorine atoms from the film, but only a comparatively small change in the carbon content. Although XPS cannot detect hydrogen atoms, the significant increase in intensity of the gas phase m/z = 2 peak (Figure 3a(ii)) during electron irradiation indicates that hydrogen is lost from the film as H$_2$(g) because of electron-stimulated C−H bond cleavage, a

8595

dx.doi.org/10.1021/am501457h | ACS Appl. Mater. Interfaces 2014, 6, 8590−8601
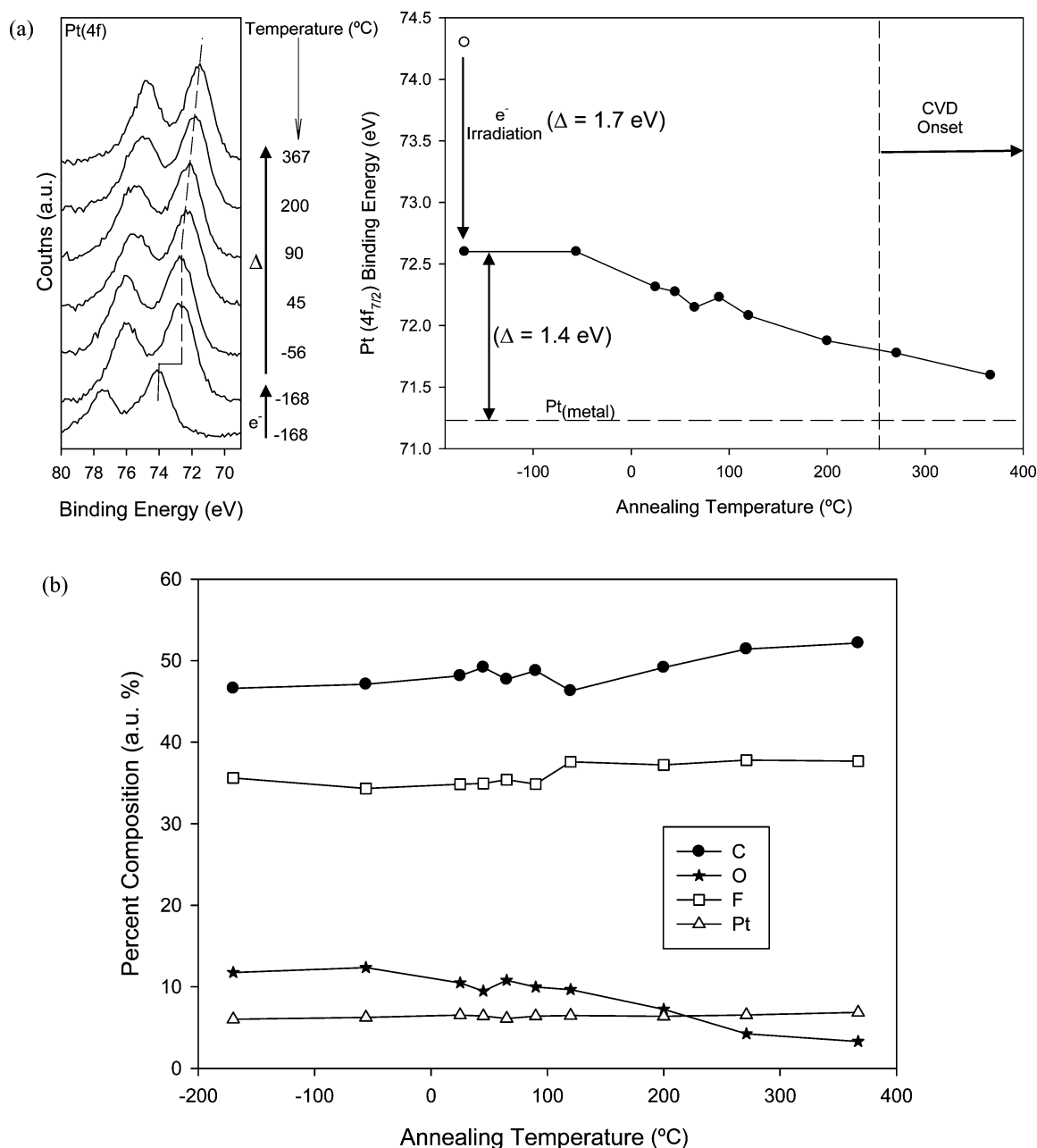
Figure 6. Effect of annealing temperature on a EBID film created by exposing a 3.30 nm thick film of $Pt^{II}(hfac)_2$ initially adsorbed at −168 °C to an electron dose of 4.50×10^{17} e⁻/cm². (a) (left) Variation in the Pt(4f) region and (right) Pt($4f_{7/2}$) peak position after electron irradiation and also as a function of the subsequent annealing temperature; in the binding energy of metallic platinum is shown as a dashed line, and the onset temperature for $Pt^{II}(hfac)_2$ CVD is also shown. (b) Change in the percent composition of carbon, oxygen, fluorine, and platinum atoms in the film.

prominent reaction pathway for adsorbed hydrocarbons exposed to electron irradiation.[53−59]

In summary, after an electron dose of ∼1×10^{17} e⁻/cm², all of the parent $Pt^{II}(hfac)_2$ molecules have decomposed, causing some of the nascent carbon, oxygen, fluorine and hydrogen atoms to be lost as CO(g)/CO_2(g), F⁻(g) and H_2(g), respectively. The residual film at this point can be best described as reduced Pt atoms encased within an amorphous carbon matrix that also contains residual oxygen and fluorine atoms. This also explains why the Pt(4f) peak position observed for the Pt_{red} species formed when $Pt^{II}(hfac)_2$ molecules decompose is not representative of platinum atoms in a fully metallic state. Pictorially this step can be represented as

Partially reduced platinum atoms in a carbonaceous matrix containing fluorine and oxygen
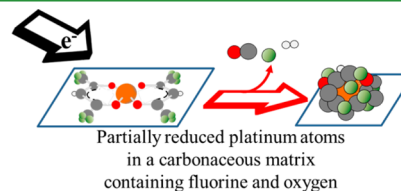
The formation of this matrix stabilizes the film toward any further carbon or oxygen desorption. Thus, for electron doses > ∼1×10^{17} e⁻/cm² the XPS and MS data in Figures 1, 2a, and 3 show that no more oxygen or carbon atoms are lost from the film, and the reduced platinum species formed during the initial stage of the reaction remain unchanged. In contrast, fluorine can continue to desorb under the influence of more sustained
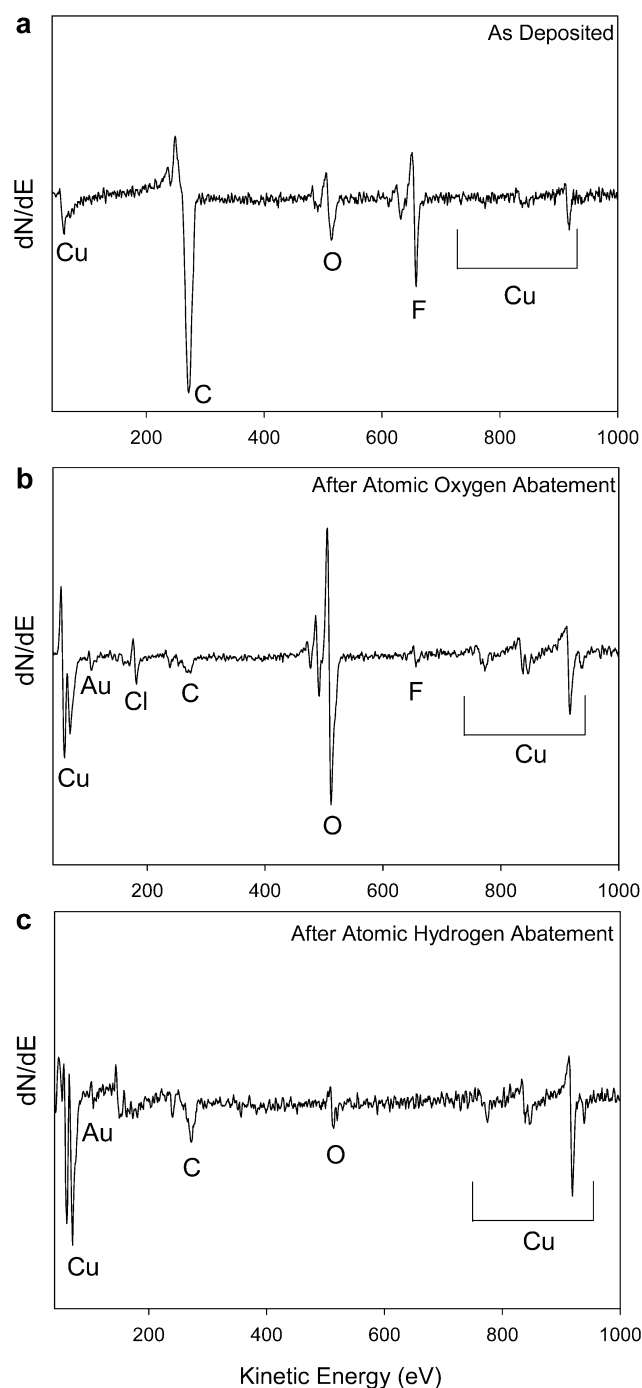
8596

dx.doi.org/10.1021/am501457h | ACS Appl. Mater. Interfaces 2014, 6, 8590−8601

Figure 7. Auger electron spectra of (a) an EBID structure created from $Cu^{II}(hfac)_2$ on a Au substrate. Deposition conditions were $P_{Cu(hfac)_2} \approx 1.0 \times 10^{-7}$ Torr, incident beam energy = 1.5 keV, substrate current ≈ 4.4 μA, deposition time 1 h; (b) the deposited structure exposed to 40 h of atomic oxygen, and then (c) exposed to 2 h of atomic hydrogen.

electron irradiation as a result of C–F bond cleavage and F$^-$ ejection. This transformation accounts not only for the sustained loss of signal in the F(1s) region for electron doses > ~1 × 10^{17} e$^-$/cm^2, but also the corresponding changes in the C(1s) region (Figure 1 and Figure S2 in the Supporting Information) as CF_2 and CF species are converted into graphitic-like, C(ads), species. This second step can be represented as
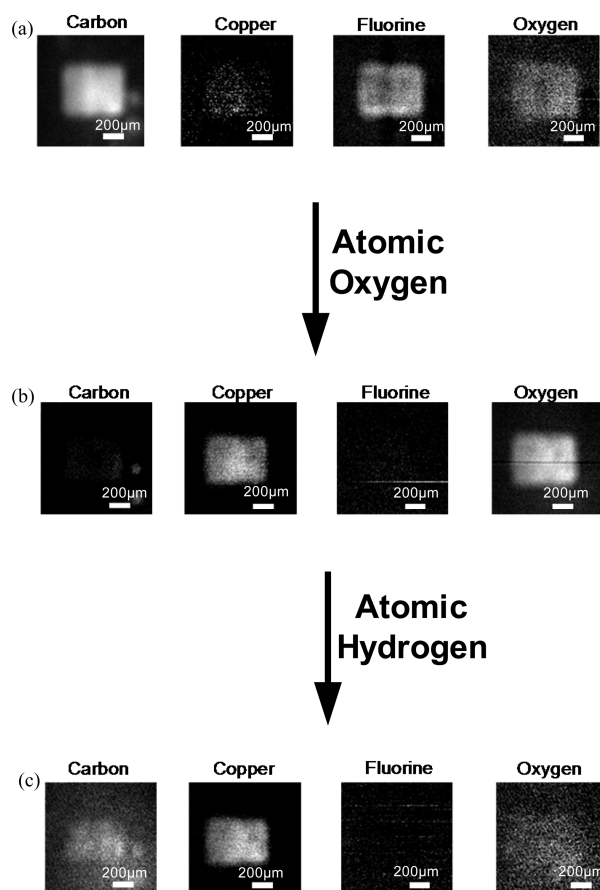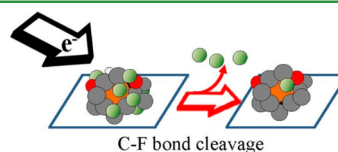

Figure 8. Auger electron elemental maps of (a) EBID films created from $Cu^{II}(hfac)_2$ on a Au substrate; deposition conditions were $P_{Cu(hfac)2} \approx 1.0 \times 10^{-7}$ Torr, incident beam energy =1.5 keV, substrate current ≈ 4.4 μA, deposition time 1 h (b) the deposited film exposed to 40 h of atomic oxygen and then, (c) exposed to 2 h of atomic hydrogen.

Analogous low-temperature UHV studies conducted with $Pd^{II}(hfac)_2$ and $Cu^{II}(hfac)_2$ reveal that similar transformations occur as a result of electron irradiation, with the loss of fluorine and oxygen, CO(g) evolution, and reduction of the metal atoms. For example, Figure S2 in the Supporting Information shows that the evolution of the C(1s) region for $Pd^{II}(hfac)_2$ exposed to electron irradiation is qualitatively similar to the changes observed for $Pt^{II}(hfac)_2$ (see Figure 1). Another example is the nature of the gas phase species produced when adsorbed $Cu^{II}(hfac)_2$ molecules were exposed to electron irradiation (compare Figure S3 in the Supporting Information and Figure 3a,ii). The one notable difference between the three metal^{II}(hfac)$_2$ complexes is the $Cu^{II}(hfac)_2$ precursor, where the electron stimulated loss of C–F bonds in the F(1s) region was accompanied by the appearance of a distinct new peak that can be identified as a fluoride ion (Figure 4).[33,46] The appearance of a fluoride (F$^-$) species can be understood by considering that electron irradiation of adsorbed $Cu^{II}(hfac)_2$ molecules creates reduced Cu species while at the same time also liberating reactive F$^-$ ions from C–F bond cleavage. Reactions between

8597

dx.doi.org/10.1021/am501457h | ACS Appl. Mater. Interfaces 2014, 6, 8590−8601

these two species produce a stable copper fluoride. In contrast to Cu, Pd and Pt do not form stable fluorides, providing a rationale for the lack of fluoride ion formation in Figure 1.[60] This behavior of $Cu^{II}(hfac)_2$ in the low-temperature UHV surface science also explains why there is a pronounced fluorine signal in the EBID structures created in the AES under steady state deposition conditions from $Cu^{II}(hfac)_2$, a feature that is all but absent in the deposits created from $Pd^{II}(hfac)_2$ and $Pt^{II}(hfac)_2$ (Figure 5).

An important difference between the EBID structures created from $Cu^{II}(hfac)_2$, $Pd^{II}(hfac)_2$, and $Pt^{II}(hfac)_2$ in the AES system (Figure 5) and the films created in the low temperature UHV studies is that the AES deposits have been subjected to much higher effective electron doses. This is a consequence of the much higher electron flux ($\sim 1 \times 10^4$) generated by the Auger electron gun ($\sim 2 \times 10^2$ $\mu A/mm^2$) compared to the broad beam electron source used in the UHV surface science experiments ($\sim 1 \times 10^{-2}$ $\mu A/mm^2$). Thus, if we extrapolate the XPS data shown in Figure 2 to the deposit that would form if a film were exposed to orders of magnitude greater electron fluxes, we would predict that EBID structures created in the AES system from $Pd^{II}(hfac)_2$, and $Pt^{II}(hfac)_2$ would contain significant amounts of carbon contamination, along with some oxygen. However, there would be little or no fluorine due to electron stimulated C−F cleavage. This is in qualitative agreement with the chemical composition of the structures made in the AES system, from $Pd^{II}(hfac)_2$ (6.5% Pd, 2.7% O, and 90.8%C) and $Pt^{II}(hfac)_2$ (3.8% Pt, 4.3% O, and 91.9% C), shown in Figure 5. As noted in the previous paragraph the presence of fluorine in films created from $Cu^{II}(hfac)_2$ is due to the formation of copper fluoride.

The similarity in the chemical composition of the EBID structures created from the three $metal^{II}(hfac)_2$ precursors, particularly the comparable concentrations of carbon and oxygen, combined with the observation that the same volatile species are detected during electron irradiation, provide strong support for the idea that the same overall deposition processes is operative for all three $metal^{II}(hfac)_2$ precursors. In contrast to previous studies on organometallic complexes that only contain monodentate ligands (e.g., $Pt(PF_3)_4$, $W(CO)_6$, and $MeCpP$-$t^{IV}Me_3$), there is no evidence of direct ligand (hfac) ejection following electron irradiation. The absence of hfac desorption can be inferred not only from the absence of any fluorine containing species in the neutrals detected by the QMS during irradiation (Figure 3), but also by the comparative lack of change in the C(1s) XPS area during irradiation and also from the preponderance of carbon in deposits created from the $metal^{II}(hfac)_2$ complexes in the AES (Figure 5) and in previous EBID studies using $Cu^{II}(hfac)_2$.[21−23,61]

The absence of any significant hfac desorption and the similar behavior of the three $metal^{II}(hfac)2$ precursors differs from recent gas-phase studies on $Cu^{II}(hfac)_2$ and $Pd^{II}(hfac)_2$. In these studies, the nature of the transition metal and the electronic structure of the complex has been shown to influence the electron interactions with $metal^{II}(hfac)_2$ complexes, including the potential for hfac ligand desorption.[29] The apparent discrepancy between these studies is a reflection of the important role that the surface can play in influencing the overall sequence of events that accompany EBID. The absence of any significant hfac desorption in this investigation and in related EBID studies can likely be attributed at least in part to the molecular weight of the hfac fragment (204 amu), which is greater than any of the central metal atoms (Cu, Pt, Pd). This

kinematic effect will reduce the nascent velocity of any hfac ligand released in a bond dissociation process and the ease with which it can "escape" from the surface and into the gas phase. Any hfac ligands released from $metal^{II}(hfac)_2$ complexes are also likely to experience significant interactions with the underlying substrate through one or both of the coordinately unsaturated oxygen atoms. Thus, hfac ligands that thermally dissociate from $Pd^{II}(hfac)_2$ on copper surfaces at low temperatures (approximately −150 °C) have been shown to remain thermally stable at 100 °C.[42] In contrast, hfac ligands released from $metal^{II}(hfac)_2$ complexes in the gas phase will not experience any of these secondary effects that must be considered in a more condensed phase medium. Unfortunately, the inability of the hfac ligands to desorb means that we cannot directly compare our results to the related gas-phase studies[29] on the same molecules to determine the role and/or relative importance of the secondary versus the primary electrons in initiating precursor decomposition. However, although our results do not allow us to unambiguously identify the initial bond dissociation event that causes the various $metal^{II}(hfac)_2$ complexes to decompose this lack of information is largely irrelevant as the fate of the carbon, oxygen, hydrogen, and fluorine atoms is effectively a consequence of how surface bound hfac ligands decompose under the influence of electron irradiation. We anticipate that a similar situation will be operative for other bulk multidentate ligands such as acac ($CH_3C=OCHC=OCH_3$) and ethylenediamine ($NH_2CH_2CH_2NH_2$), with the ejection of only small organic fragments during EBID. In support of this assertion, CO and CH_4/CH_3 were the only volatile carbon-containing fragment produced when adsorbed $Me_2Au(acac)$ molecules were electron irradiated.[39] The one aspect of the dissociation/deposition process where the central metal atom does seem to play a role is in the secondary reactions that can occur between the partially reduced metal atoms liberated in the initial decomposition step and volatile fragments generated as the ligands decompose.

Post-deposition Abatement. In this study, we also evaluated the effect of two post-deposition abatement strategies, annealing and exposure to atomic radicals, on the chemical composition of and bonding in EBID structures created from $metal^{II}(hfac)_2$ precursors.

Figure 6 shows the effect of annealing an EBID film initially created from $Pt^{II}(hfac)_2$ at −168 °C. On the basis of the initial electron dose (4.50×10^{17} e^-/cm^2) this film is initially composed of reduced platinum atoms, encased in a carbon matrix that also contains some residual oxygen and fluorine atoms. Figure 6b shows that oxygen is lost (from 11 atomic % to 3 atomic %) when the substrate is annealed above 100 °C. However, increasing the substrate temperature produced no change in the carbon or fluorine content. For fluorine this in contrast to the effect of electron irradiation due to the fact that while C−F bonds are labile toward electrons they are thermally inert (C−F bond strength $\approx$ 490 kJ/mol).[20] Increasing the substrate temperature above room temperature is also seen to produce a systematic decrease in the $Pt(4f_{7/2})$ binding energy (Figure 6a), indicative of the platinum atoms becoming more metallic. The correlation between the loss of oxygen from the film that occurs upon annealing (Figure 6b) and the decrease in $Pt(4f_{7/2})$ binding energy (Figure 6a) suggests that Pt−O bonds are initially present in the as deposited structures. This possibility is reasonable given the presence of M−O bonds in the parent $metal^{II}(hfac)_2$ molecules. Moreover, the loss of

oxygen between 0−400 °C is in line with the thermal stability of Pt−O bonds formed on Pt nanoparticles.[62] Previous studies on EBID deposits formed from MeCpPtMe$_3$, however, have also reported a decrease in Pt(4f$_{7/2}$) binding energy of a similar magnitude to the one shown in Figure 6 and over a similar temperature range in a situation where no Pt−O bonds could be present.[36] In this case, the decrease in platinum binding energy was attributed to the effect of metal atom coalescence promoted by increased metal atom diffusion in the carbonaceous matrix at higher substrate temperatures. Our results do not allow us to say unambiguously if one or both of these two effects (Pt−O bond cleavage or metal atom coalescence) is responsible for the decrease in Pt binding energy, although Figure 6 demonstrates that increasing the substrate temperature during EBID or post deposition annealing have the potential to improve certain material properties (e.g., resistivity). It should be noted that if elevated substrate temperatures are used during deposition they should not exceed ∼250 °C, the onset of conformal CVD from Pt^{II}(hfac)$_2$.[24,63] We anticipate that similar benefits should also occur for EBID nanostructures created from Pd^{II}(hfac)$_2$ or Cu^{II}(hfac)$_2$, provided that the onset temperatures for CVD are not breeched.

The second abatement strategy investigated was the effect of exposing EBID structures created from Cu^{II}(hfac)$_2$ to atomic oxygen (AO) and then atomic hydrogen (AH). Atomic radicals are a potentially useful means of abating organic contaminants because they possess a high degree of intrinsic chemical reactivity and etching ability, but in contrast to ion beams, lack the ability to sputter metal atoms.[64−66] Figures 7b and 8b show that AO can etch virtually all of the carbon and fluorine atoms from an EBID structure created from Cu^{II}(hfac)$_2$, causing an AES signal from the Au substrate to appear in Figure 7b. After AO exposure the deposit consists almost exclusively of copper oxide, which Figures 7c and 8c show can be reduced to metallic copper by exposure to atomic hydrogen (AH). Thus, the combination of AO followed by AH exposure effectively removes almost all of the organic contaminants, analogous to our observations on EBID structures created from Me$_2$Au-(acac).[28] In our previous studies, Atomic Force Microscopy (AFM) revealed that at a microscopic level the EBID deposits created in the AES system from Me$_2$Au(acac), and by inference also from Cu^{II}(hfac)$_2$, consist of closely packed discrete spherical particles. Upon exposure to AO and AH the size of these objects, as measured by their height in AFM, decreased to an extent that was consistent with the residual gold atoms being present in a close packed arrangement.[28] Interestingly, an analogous result has recently been obtained in a study on the post deposition abatement of carbon from EBID structures created from MeCpPtMe$_3$ using oxygen gas in the presence of an electron beam. In this recent investigation by Plank et al. the active species responsible for carbon etching are presumably also reactive oxygen species (ROS) generated by the electron stimulated decomposition of molecular oxygen, most likely atomic oxygen.[27] If these ROS-based remediation strategies are proven capable of removing the organic contamination, while the remaining structure forms a compact and close-packed arrangement of metal atoms as opposed to a honeycomb structure, then they have significant potential in EBID as a post deposition strategy.

5. CONCLUSIONS

The electron-stimulated reactions of surface bound metal^{II}(hfac)$_2$ complexes proceeds by the decomposition of hfac

ligands, leading to the ejection of volatile species such as CO(g) and F$^-$(g). As a consequence, carbon is the overwhelming (≳ 90%) form of organic contamination left in EBID nanostructures created from metal^{II}(hfac)$_2$ precursors, although fluorine atoms are largely absent because of their effective removal by electron-stimulated C−F bond cleavage. The absence of any hfac ligand desorption is ascribed to the inability of the bulky and coordinatively unsaturated hfac ligands to desorb, even if they are released from metal^{II}(hfac)$_2$ complexes by electron stimulated processes. As a result, the central metal atom's identity is largely irrelevant in the precursor's surface reactions. The central metal atom, can, however, play a role in regulating secondary reactions, as evidenced by the formation of copper fluoride during the electron stimulated reactions of adsorbed Cu^{II}(hfac)$_2$ molecules. Post-deposition annealing of EBID structures created from metal^{II}(hfac)$_2$ increases the film's metallic character, as a result of oxygen desorption and/or enhanced metal atom mobility. Under ambient temperatures, post-deposition purification of EBID structures can be achieved by exposing them to atomic oxygen, creating a metal oxide, which can then be reduced to the pure metal by atomic hydrogen.

■ ASSOCIATED CONTENT

ⓢ Supporting Information

Figure S1: Evolution of the Pt(4f), C(1s), O(1s), and F(1s) XP regions for a 4.0 nm thick film of Pt^{II}(hfac)$_2$ irradiated with X-rays (Mg Kα 1253.6 eV); Figure S2: (a) Evolution of the C(1s) XP region for thick films (>5.0 nm) of Pd^{II}(hfac)$_2$ adsorbed to an (a:C) substrate at −100 °C, exposed to electron irradiation. Figure S3: Mass spectrum (0−100 amu) of the volatile neutral species produced when a ∼ 2.5 nm film of Cu^{II}(hfac)$_2$ adsorbed onto an (a:C) substrate at −110 °C was irradiated for the first 0−20 s. This material is available free of charge via the Internet at http://pubs.acs.org/.

■ AUTHOR INFORMATION

Corresponding Author

*E-mail: howardf@jhu.edu.

Notes

The authors declare no competing financial interest.

■ ACKNOWLEDGMENTS

■ REFERENCES

(1) Botman, A.; Mulders, J. J. L.; Hagen, C. W. Creating Pure Nanostructures From Electron-Beam-Induced Deposition Using Purification Techniques: A Technology Perspective. *Nanotechnology* **2009**, *20* (37), 37200/1−372001/17.

(2) Huth, M.; Porrati, F.; Schwalb, C.; Winhold, M.; Sachser, R.; Dukic, M.; Adams, J.; Fantner, G. Focused Electron Beam Induced Deposition: A Perspective. *Beilstein J. Nanotechnol.* **2012**, *3*, 597−619.

(3) Utke, I.; Hoffmann, P.; Melngailis, J. Gas-Assisted Focused Electron Beam and Ion Beam Processing and Fabrication. *J. Vac. Sci. Technol. B* **2008**, *26* (4), 1197−1276.

(4) van Dorp, W. F.; Hagen, C. W. A Critical Literature Review of Focused Electron Beam Induced Deposition. *J. Appl. Phys.* **2008**, *104* (8), 081301/1−081301/42.

(5) Botman, A.; Hesselberth, M.; Mulders, J. J. L. Improving the Conductivity of Platinum-Containing Nano-Structures Created by Electron-Beam-Induced Deposition. *Microelectron. Eng.* **2008**, *85* (5−6), 1139−1142.

(6) Botman, A.; Mulders, J. J. L.; Weemaes, R.; Mentink, S. Purification of Platinum and Gold Structures after Electron-Beam-Induced Deposition. *Nanotechnology* **2006**, *17* (15), 3779−3785.

(7) Koops, H. W. P.; Kaya, A.; Weber, M. Fabrication and Characterization of Platinum Nanocrystalline Material Grown by Electron-Beam Induced Deposition. *J. Vac. Sci. Technol. B* **1995**, *13* (6), 2400−2403.

(8) Utke, I.; Friedli, V.; Michler, J.; Bret, T.; Multone, X.; Hoffmann, P. Density Determination of Focused-Electron-Beam-Induced Deposits with Simple Cantilever-Based Method. *Appl. Phys. Lett.* **2006**, *88* (3), 031906/1−031906/3.

(9) Fernandez-Pacheco, A.; De Teresa, J. M.; Cordoba, R.; Ibarra, M. R. Magnetotransport Properties of High-Quality Cobalt Nanowires Grown by Focused-Electron-Beam-Induced Deposition. *J. Phys. D Appl. Phys.* **2009**, *42* (5), 055005/1−055005/6.

(10) Lau, Y. M.; Chee, P. C.; Thong, J. T. L.; Ng, V. Properties and Applications of Cobalt-Based Material Produced by Electron-Beam-Induced Deposition. *J. Vac. Sci. Technol. A* **2002**, *20* (4), 1295−1302.

(11) Serrano-Ramon, L.; Cordoba, R.; Rodriguez, L. A.; Magen, C.; Snoeck, E.; Gatel, C.; Serrano, I.; Ibarra, M. R.; De Teresa, J. M. Ultrasmall Functional Ferromagnetic Nanostructures Grown by Focused Electron-Beam-Induced Deposition. *Nano* **2011**, *5* (10), 7781−7787.

(12) Zhang, W.; Shimojo, M.; Takeguchi, M.; Furuya, K. Electron Beam-Induced Formation Of Nanosized Alpha-Fe Crystals. *J. Mater. Sci.* **2006**, *41* (9), 2577−2580.

(13) Gazzadi, G.; Mulders, H.; Trompenaars, P.; Ghirri, A.; Affronte, M.; Grillo, V.; Frabboni, S. Focused Electron Beam Deposition of Nanowires from Cobalt Tricarbonyl Nitrosyl $(Co(CO)_3NO)$ Precursor. *J. Phys. Chem. C* **2011**, *115*, 19606−19611.

(14) Utke, I.; Hoffmann, P.; Berger, R.; Scandella, L. High-Resolution Magnetic Co Supertips Grown by a Focused Electron Beam. *Appl. Phys. Lett.* **2002**, *80* (25), 4792−4794.

(15) Sharma, R.; Moore, E.; Rez, P.; Treacy, M. M. J. Site-Specific Fabrication of Fe Particles for Carbon Nanotube Growth. *Nano Lett.* **2009**, *9* (2), 689−694.

(16) Ervin, M. H.; Nichols, B. M. Electron Beam Induced Deposition of Cobalt for Use as Single- And Multiwalled Carbon Nanotube Growth Catalyst. *J. Vac. Sci. Technol. B* **2009**, *27* (6), 2982−2985.

(17) Bauerdick, S.; Linden, A.; Stampfer, C.; Helbling, T.; Hierold, C. Direct Wiring Of Carbon Nanotubes For Integration In Nano-electromechanical Systems. *J. Vac. Sci. Technol. B* **2006**, *24* (6), 3144−3147.

(18) Liang, T.; Frendberg, E.; Lieberman, B.; Stivers, A. Advanced Photolithographic Mask Repair Using Electron Beams. *J. Vac. Sci. Technol. B* **2005**, *23* (6), 3101−3105.

(19) Edinger, K.; Becht, H.; Bihr, J.; Boegli, V.; Budach, M.; Hofmann, T.; Koops, H. W. P.; Kuschnerus, P.; Oster, J.; Spies, P.; Weyrauch, B. Electron-Beam-Based Photomask Repair. *J. Vac. Sci. Technol. B* **2004**, *22* (6), 2902−2906.

(20) Bruice, P. Y. *Organic Chemistry*, 6th ed.; Prentice Hall: Upper Saddle River, NJ, 2010.

(21) Cohen, S. L.; Liehr, M.; Kasi, S. Mechanisms of Copper Chemical Vapor-Deposition. *Appl. Phys. Lett.* **1992**, *60* (1), 50−52.

(22) Luisier, A.; Utke, I.; Bret, T.; Cicoira, F.; Hauert, R.; Rhee, S. W.; Doppelt, P.; Hoffmann, P. Comparative Study Of Cu-Precursors For 3D Focused Electron Beam Induced Deposition. *J. Electrochem. Soc.* **2004**, *151* (9), C590−C593.

(23) Miyazoe, H.; Utke, I.; Kikuchi, H.; Kiriu, S.; Friedli, V.; Michler, J.; Terashima, K. Improving The Metallic Content Of Focused Electron Beam-Induced Deposits by a Scanning Electron Microscope Integrated Hydrogen-Argon Microplasma Generator. *J. Vac. Sci. Technol. B* **2010**, *28* (4), 744−750.

(24) Jeon, N. L.; Lin, W.; Erhardt, M. K.; Girolami, G. S.; Nuzzo, R. G. Selective Chemical Vapor Deposition of Platinum and Palladium Directed by Monolayers Patterned Using Microcontact Printing. *Langmuir* **1997**, *13* (14), 3833−3838.

(25) Mulders, J. J. L.; Belova, L. M.; Riazanova, A. Electron Beam Induced Deposition at Elevated Temperatures: Compositional

(26) Roberts, N. A.; Fowlkes, J. D.; Magel, G. A.; Rack, P. D. Enhanced Material Purity and Resolution Via Synchronized Laser Assisted Electron Beam Induced Deposition of Platinum. *Nanoscale* **2013**, *5* (1), 408−415.

(27) Plank, H.; Noh, J. H.; Fowlkes, J. D.; Lester, K.; Lewis, B. B.; Rack, P. D. Electron-Beam-Assisted Oxygen Purification at Low Temperatures for Electron-Beam-Induced Pt Deposits: Towards Pure and High-Fidelity Nanostructures. *ACS Appl. Mater. Interfaces* **2014**, *6* (2), 1018−1024.

(28) Wnuk, J. D.; Gorham, J. M.; Rosenberg, S. G.; Madey, T. E.; Hagen, C. W.; Fairbrother, D. H. Atomic Radical Abatement of Organic Impurities from Electron Beam Deposited Metallic Structures. *J. Vac. Sci. Technol. B* **2010**, *28* (3), 527−537.

(29) Engmann, S.; Omarsson, B.; Lacko, M.; Stano, M.; Matejcik, S.; Ingolfsson, O. Dissociative Electron Attachment to Hexafluoroacety-lacetone and Its Bidentate Metal Complexes $M(hfac)_2$; M = Cu, Pd. *J. Chem. Phys.* **2013**, *138* (23), 234309/1−234309/9.

(30) Smith, D. A.; Fowlkes, J. D.; Rack, P. D. A Nanoscale Three-Dimensional Monte Carlo Simulation of Electron-Beam-Induced Deposition with Gas Dynamics. *Nanotechnology* **2007**, *18* (26), 265308/1−265308/14.

(31) Silvis-Cividjian, N.; Hagen, C. W.; Kruit, P.; Van der Stam, M. A. J.; Groen, H. B. Direct Fabrication Of Nanowires In An Electron Microscope. *Appl. Phys. Lett.* **2003**, *82* (20), 3514−3516.

(32) Landheer, K.; Rosenberg, S. G.; Bernau, L.; Swiderek, P.; Utke, I.; Hagen, C. W.; Fairbrother, D. H. Low-Energy Electron-Induced Decomposition and Reactions of Adsorbed Tetrakis-(trifluorophosphine)platinum $[Pt(PF_3)_4]$. *J. Phys. Chem. C* **2011**, *115* (35), 17452−17463.

(33) Perry, C. C.; Torres, J.; Carlo, S. R.; Fairbrother, D. H. Reactivity Of Cu With Poly(Tetrafluoroethylene) and Poly(Vinyl Chloride): Effect of Pre- and Post-Metallization Modification on the Metal/Polymer Interface. *J. Vac. Sci. Technol. A* **2002**, *20* (5), 1690−1698.

(34) Rosenberg, S. G.; Barclay, M.; Fairbrother, D. H. Electron Induced Reactions of Surface Adsorbed Tungsten Hexacarbonyl $(W(CO)_6)$. *Phys. Chem. Chem. Phys.* **2013**, *15* (11), 4002−4015.

(35) Rosenberg, S. G.; Barclay, M.; Fairbrother, D. H. Electron Beam Induced Reactions of Adsorbed Cobalt Tricarbonyl Nitrosyl (Co-$(CO)_3NO)$ Molecules. *J. Phys. Chem. C* **2013**, *117* (31), 16053−16064.

(36) Rosenberg, S. G.; Landheer, K.; Hagen, C. W.; Fairbrother, D. H. Substrate Temperature And Electron Fluence Effects on Metallic Films Created by Electron Beam Induced Deposition. *J. Vac. Sci. Technol. B* **2012**, *30* (5), 051805/1−051805/10.

(37) van Dorp, W. F.; Wnuk, J. D.; Gorham, J. M.; Fairbrother, D. H.; Madey, T. E.; Hagen, C. W. Electron Induced Dissociation of Trimethyl(methylcyclopentadienyl)platinum(IV): Total Cross Section as a Function of Incident Electron Energy. *J. Appl. Phys.* **2009**, *106* (7), 074901/1−074903/9.

(38) Wnuk, J. D.; Gorham, J. M.; Rosenberg, S. G.; van Dorp, W. F.; Madey, T. E.; Hagen, C. W.; Fairbrother, D. H. Electron Induced Surface Reactions of the Organometallic Precursor Trimethyl-(methylcyclopentadienyl)platinum(IV). *J. Phys. Chem. C* **2009**, *113* (6), 2487−2496.

(39) Wnuk, J. D.; Gorham, J. M.; Rosenberg, S. G.; van Dorp, W. F.; Madey, T. E.; Hagen, C. W.; Fairbrother, D. H. Electron Beam Irradiation of Dimethyl-(acetylacetonate) Gold(III) Adsorbed Onto Solid Substrates. *J. Appl. Phys.* **2010**, *107* (5), 054301/1−054301/11.

(40) Wnuk, J. D.; Rosenberg, S. G.; Gorham, J. M.; van Dorp, W. F.; Hagen, C. W.; Fairbrother, D. H. Electron Beam Deposition for Nanofabrication: Insights from Surface Science. *Surf. Sci.* **2011**, *605* (3−4), 257−266.

(41) Wnuk, J. D.; Gorham, J. M.; Rosenberg, S. G.; van Dorp, W. F.; Madey, T. E.; Hagen, C. W.; Fairbrother, D. H., Electron beam irradiation of dimethyl-(acetylacetonate) gold(III) adsorbed onto solid substrates. *J. Appl. Phys.* **2010**, *107*, (5).

(42) Lin, W.; Wiegand, B. C.; Nuzzo, R. G.; Girolami, G. S. Mechanistic Studies of Palladium Thin Film Growth from Palladium-(II) b-Diketonates. 1. Spectroscopic Studies on the Reactions of Bis(hexafluoroacetylacetonato)palladium(II) on Copper Surfaces. *J. Am. Chem. Soc.* **1996**, *118*, 5977−5987.

(43) Moulder, J. F.; Stickle, W. F.; Sobol, P. E.; Bomben, K. E. *Handbook of X-ray Photoelectron Spectroscopy*; Physical Electronics USA: Chanhassen, MN, 1995.

(44) Tanuma, S.; Powell, C. J.; Penn, D. R. Calculations of Electron Inelastic Mean Free Paths 0.2. Data for 27 Elements over the 50−2000-Ev Range. *Surf. Interface Anal.* **1991**, *17* (13), 911−926.

(45) NIST Mass Spectrometry Data Center. http://webbook.nist.gov/cgi/cbook.cgi?ID=C14781454&Units=SI&Mask=200#Mass-Spec (January 7 2013).

(46) Vanderlaan, G.; Westra, C.; Haas, C.; Sawatzky, G. A. Satellite Structure in Photoelectron and Auger-Spectra of Copper Dihalides. *Phys. Rev. B* **1981**, *23* (9), 4369−4380.

(47) Wagner, A. J.; Han, K.; Vaught, A. L.; Fairbrother, D. H. X-ray Induced Modification of Semifluorinated Organic Thin Films. *J. Phys. Chem. B* **2000**, *104* (14), 3291−3297.

(48) Wagner, A. J.; Vecitis, C. D.; Fairbrother, D. H. $CF_3(CF_2)_7(CH_2)_2SH$ self-assembled on Au and subsequent degradation under the influence of ionizing radiation as measured by XPS. *Surface Science Spectra* **2001**, *8* (1), 32−38.

(49) Perry, C. C.; Wagner, A. J.; Fairbrother, D. H. Electron stimulated C-F bond breaking kinetics in fluorine-containing organic thin films. *Chem. Phys.* **2002**, *280* (1−2), 111−118.

(50) Graham, R. L.; Bain, C. D.; Biebuyck, H. A.; Laibinis, P. E.; Whitesides, G. M. Damage To Trifluoroacetamido-Terminated Organic Self-Assembled Monolayers (SAMs) on Aluminum, Titanium, Copper and Gold by Aluminum Kα X-Rays Is due Principally to Electrons. *J. Phys. Chem.* **1993**, *97* (37), 9456−9464.

(51) Laibinis, P. E.; Graham, R. L.; Biebuyck, H. A.; Whitesides, G. M. X-Ray Damage to Trifluoroacetoxy-Terminated Organic Monolayers on Silicon/Gold: Principal Effect of Electrons. *Science* **1991**, *254* (5034), 981−983.

(52) Badey, J. P.; Espuche, E.; Jugnet, Y.; Chabert, B.; Duc, T. M. Influence of Chemical and Plasma Treatments on the Adhesive Properties of PTFE with an Epoxy Resin. *Int. J. Adhes. Adhes.* **1996**, *16* (3), 173−178.

(53) Davies, B. M.; Craig, J. H. Electron-Beam-Induced Decomposition of Trimethylamine on Si(100)-2 × 1. *Surf. Interface Anal.* **2003**, *35* (13), 1060−1064.

(54) Lozano, J.; Early, D.; Craig, J. H.; Wang, P. W.; Kimberlin, K. R. HREELS, TPD and ESD Study of Electron-Induced Decomposition of Trimethylamine on Si(100) at 100 K. *Surf. Interface Anal.* **2005**, *37* (4), 366−373.

(55) Xu, C.; Koel, B. E. Electron-Induced Dissociation of Hydrocarbon Multilayers. *Surf. Sci.* **1993**, *292* (1−2), L803−L809.

(56) Seshadri, K.; Froyd, K.; Parikh, A. N.; Allara, D. L.; Lercel, M. J.; Craighead, H. G. Electron-Beam-Induced Damage in Self-Assembled Monolayers. *J. Phys. Chem.* **1996**, *100* (39), 15900−15909.

(57) Rowntree, P.; Dugal, P. C.; Hunting, D.; Sanche, L. Electron Stimulated Desorption of H_2 from Chemisorbed Molecular Monolayers. *J. Phys. Chem.* **1996**, *100* (11), 4546−4550.

(58) Olsen, C.; Rowntree, P. A. Bond-Selective Dissociation of Alkanethiol Based Self-Assembled Monolayers Absorbed on Gold Substrates, Using Low-Energy Electron Beams. *J. Chem. Phys.* **1998**, *108* (9), 3750−3764.

(59) Huels, M. A.; Dugal, P. C.; Sanche, L. Degradation of Functionalized Alkanethiolate Monolayers by 0−18 eV Electrons. *J. Chem. Phys.* **2003**, *118* (24), 11168−11178.

(60) Miessler, G. L.; Fischer, P. J.; Tarr, D. A. *Inorganic Chemistry*, 5th ed.; Pearson: Malaysia, 2013.

(61) Utke, I.; Luisier, A.; Hoffmann, P.; Laub, D.; Buffat, P. A. Focused-Electron-Beam-Induced Deposition of Freestanding Three-Dimensional Nanostructures of Pure Coalesced Copper Crystals. *Appl. Phys. Lett.* **2002**, *81* (17), 3245−3247.

(62) Ono, L. K.; Yuan, B.; Heinrich, H.; Cuenya, B. R. Formation and Thermal Stability of Platinum Oxides on Size-Selected Platinum Nanoparticles: Support Effects. *J. Phys. Chem. C* **2010**, *114* (50), 22119−22133.

(63) Utriainen, M.; Kroger-Laukkanen, M.; Johansson, L. S.; Niinisto, L. Studies of Metallic Thin Film Growth in an Atomic Layer Epitaxy Reactor Using M(acac)$_2$ (M = Ni, Cu, Pt) Precursors. *Appl. Surf. Sci.* **2000**, *157* (3), 151−158.

(64) Bischler, U.; Bertel, E. Simple Source of Atomic Hydrogen for Ultrahigh Vacuum Applications. *J. Vac. Sci. Technol. A* **1993**, *11* (2), 458−460.

(65) Tomkiewicz, P.; Winkler, A.; Krzywiecki, M.; Chasse, T.; Szuber, J. Analysis of Mechanism of Carbon Removal from Gaas Surface by Atomic Hydrogen. *Appl. Surf. Sci.* **2008**, *254* (24), 8035−8040.

(66) Blackwood, J.; McTaggart, F. The oxidation of Carbon with Atomic Oxygen. *Aust. J. Chem.* **1959**, *12* (2), 114−121.